





Article

Increasing Light-Induced Forces with Magnetic Photonic Glasses

Hugo Avalos-Sánchez ¹, Abraham J. Carmona-Carmona ¹ , Martha A. Palomino-Ovando ¹, Benito Flores Desirena ¹, Rodolfo Palomino-Merino ¹, Khashayar Misaghian ^{2,3} , Jocelyn Faubert ² , Miller Toledo-Solano ^{3,*}  and Jesus Eduardo Lugo ^{1,2,4,*}

- ¹ Facultad de Ciencias Físico-Matemáticas, Benemérita Universidad Autónoma de Puebla, Av. San Claudio y Av. 18 sur, Col. San Manuel Ciudad Universitaria, Puebla Pue 72570, Mexico; hugo.avaloss@alumno.buap.mx (H.A.-S.); abraham.carmona@fcfm.buap.mx (A.J.C.-C.); marthap@fcfm.buap.mx (M.A.P.-O.); bflores@fcfm.buap.mx (B.F.D.); palomino@fcfm.buap.mx (R.P.-M.)
- ² Faubert Lab, Ecole d'optométrie, Université de Montréal, Montréal, QC H3T1P1, Canada; k.misaghian@sagesentinel.com (K.M.); jocelyn.faubert@umontreal.ca (J.F.)
- ³ CONAHCYT-Facultad de Ciencias Físico-Matemáticas, Benemérita Universidad Autónoma de Puebla, Av. San Claudio y Av. 18 sur, Col. San Manuel Ciudad Universitaria, Puebla Pue 72570, Mexico
- ⁴ Sage-Sentinel Smart Solutions, 1919-1 Tancha, Onna-son Kunigami-gun, Okinawa 904-0495, Japan
- * Correspondence: mtoledoso@conahcyt.mx (M.T.-S.); eduardo.lugo@sagesentinel.com (J.E.L.)

Abstract: In this work, we theoretically and experimentally study the induction of electromagnetic forces in an opal-based magnetic photonic glass, where light normally impinges onto a disordered arrangement of SiO₂ spheres by the aggregation of Fe₃O₄ nanoparticles. The working wavelength is 633 nm. Experimental evidence is presented for the force that results from forced oscillations of the photonic structure. Finite-element method simulations and a theoretical model estimate the magnetic force volumetric density value, peak displacement, and velocity of oscillations. The magnetic force is of the order of 56 microN, which is approximately 500-times higher than forces induced in dielectric optomechanical photonic crystal cavities.

Keywords: photonic crystal; dielectric; electromagnetic forces; opal; Fe₃O₄



Citation: Avalos-Sánchez, H.; Carmona-Carmona, A.J.; Palomino-Ovando, M.A.; Desirena, B.F.; Palomino-Merino, R.; Misaghian, K.; Faubert, J.; Toledo-Solano, M.; Lugo, J.E. Increasing Light-Induced Forces with Magnetic Photonic Glasses. *Photonics* **2024**, *11*, 827. <https://doi.org/10.3390/photonics11090827>

Received: 17 June 2024

Revised: 25 August 2024

Accepted: 30 August 2024

Published: 1 September 2024



Copyright: © 2024 by the authors. Licensee MDPI, Basel, Switzerland. This article is an open access article distributed under the terms and conditions of the Creative Commons Attribution (CC BY) license (<https://creativecommons.org/licenses/by/4.0/>).

1. Introduction

Photonic crystals (PCs) are commonly made from periodic materials [1] that alter the propagation of photons, and sometimes PCs are built up from nanostructures [2]. Light with wavelengths that can pass through the structure are known as extended photonic modes, which create photonic bands. Prohibited bands of specific wavelengths are known as photonic bandgaps (PBGs). PBGs give rise to different optical phenomena, such as high-reflectivity omnidirectional mirrors [3], Bloch oscillations [4,5], sensing [6], negative refraction [7], and localization of photons [8]. In past years, a line of research that has begun to be exploited is related to combining PCs with other materials to create new devices. Redshift and polarization-sensitive PBGs can be found in one-dimensional PCs (1D-PCs) containing hyperbolic or elliptical metamaterials [9,10]. Moreover, two-dimensional PCs (2D-PCs) show better decoupling in light-emitting diodes [11], functioning as powerful light sources [12,13] with high efficiency [11]. Additionally, three-dimensional PCs (3D-PCs) have found applications in optoelectronics [14] and thermal photovoltaic cells [15].

In recent years, the influence of magnetic materials embedded in PCs on the optical and magnetic properties of synthesized composites has been reported in many investigations. These materials, known as magnetic photonic crystals (MPCs), break time inversion symmetry, allowing nonreciprocal effects in light propagation [16,17] and additionally allowing light to be slowed at frequencies close to photonic band edges, enormously increasing the light-matter interaction and enhancing the magneto-optical response [18–20]. Thus, MPCs have potential applications in magneto-optical devices such as isolators and

circulators [21–24], as wideband ideal optical diodes [25], or for enhanced light–matter interactions [26], among others.

Meanwhile, photonic crystals (PCs) exploit the periodicity in the dielectric constant and the consequent long-range correlation; disordered structures can still strongly affect light transport [27]. For example, in structures known as photonic glasses (PGs), which are composed of disordered configurations of identical building blocks, the transport velocity of light can be significantly reduced at specific wavelengths [28], and random lasing can be controlled [29]. This PG class may generate a wide spectral range of purely structural, angular-independent colors and could be the key to optimizing tunable photonic materials [30]. Additionally, they are central to understanding fundamental questions such as isotropic structural colors, random lasing, and strong light localization in three dimensions [31].

On the other hand, the manipulation of micro-objects and biological organisms has been achieved by utilizing radiation pressure. Optical traps have been developed based on the force of radiation pressure that results from photon momentum transfer. These traps include early optical levitation configurations and optical tweezers [32,33]. A micromechanical resonator has been created, directly operated through radiation pressure [34]. Optical microcavities in optomechanics utilize radiation pressure to couple light and matter, while the optical gradient force is the driving force. The resonator displacement and laser intensity heavily influence the strength of the optical gradient force [35,36]. Experimental evidence has shown that photonic microcavities can undergo self-oscillations and forced oscillations due to radiation pressure [37–39]. Radiation pressures of the order 36.67 mN/m^2 and forces of 110 nN were achieved [38]; traditionally, dielectric optomechanical photonic crystal cavities generate forces of the order of tenths of nN [40]. However, adding a magnetic material may increase these forces, and the electromagnetic force can be demonstrated through forced or self-oscillations.

In this article, we researched experimentally the induction of electromagnetic forces in magnetic photonic glasses (MPGs) based on SiO_2 artificial opals [41–46] infiltrated with Fe_3O_4 superparamagnetic nanoparticles (NPs). Theoretically, the mean force present in our system is magnetic. Its volumetric density is given by $\vec{f} = \nabla(\vec{M} \cdot \vec{B})$, where \vec{M} is the magnetization, and \vec{B} is the magnetic flux density. The fabrication process of the magnetic glass is simpler than using other materials. For instance, if porous silicon is used, it requires creating it out of crystalline silicon first and then infiltrating it with magnetic nanoparticles. In our present case, only one step is necessary. The MPGs were obtained using the co-assembly method [47], which previously has been employed by some of us [48,49]. However, MPCs consisting of SiO_2 spheres embedded with Fe_3O_4 superparamagnetic NPs can also be obtained [50]. Since the exact formulation of the force exerted by electromagnetic fields within media remains controversial and unclear [51,52], to gain insight into the induction of electromagnetic force on the MPGs, we directed laser light with a wavelength of 633 nm perpendicularly onto beam shape MPGs. Experimental evidence demonstrates the electromagnetic force generated when the MPGs undergo forced oscillations. We quantified maximum displacement and velocity of $7.9 \text{ }\mu\text{m}$ and 3.42 mm/s , respectively, for an external frequency of 69 Hz. Using Finite-Element Method (FEM) simulations, we calculated the maximum displacement caused by the magnetic force. We then analyzed a dynamic model for forced mechanical oscillations of the MPGs. We found that MPG materials can significantly enhance the magnetic forces in these structures, which builds upon our previous research results. Our research can enhance the comprehension of magnetic forces in MPGs, propose possible uses in controlling micro-objects through radiation pressure, and create opportunities for additional advancements. For example, in energy harvesters, by utilizing sunlight in place of a laser, the oscillations of the MPG generate voltages in a coil, which can then be stored.

The present work is organized as follows. In Section 2, we describe the materials and methods. We present the experimental details to fabricate the MPGs, their characterization, the mechanical oscillation measurements, the FEM simulation parameters for the maximum

oscillation amplitude, and the theoretical model for mechanical oscillations. In Section 3, we present all the results, including the samples' structural, optical, and magnetic properties. The experimental measurements of the MPGs' oscillations are compared with the theoretical model for forced mechanical oscillations. In Section 4, we discuss all the results. Lastly, we provide concluding remarks and outline our future work in Section 5.

2. Materials and Methods

2.1. Preparation of MPGs

The process described by Sanchez et al. [53] was used to synthesize the magnetite NPs and SiO₂ spheres. MPG films were obtained according to the procedure reported by Cong et al. [47]. These were prepared using a glass substrate of dimensions $10 \times 25 \times 1.5 \text{ mm}^3$, which was treated previously to create a clean and hydrophilic surface. It was dipped vertically into a 30 mL beaker containing 15 mL of the colloidal suspension of SiO₂ spheres (0.080 g in 15 mL deoxygenated deionized water) and 1 mL of a suspension of Fe₃O₄ NPs (0.4004 g in 30 mL deoxygenated deionized water) at a temperature of 80 °C for eight hours in a drying oven. After the evaporation of water, a disordered arrangement of SiO₂ spheres was obtained due to the aggregation of NPs Fe₃O₄, which formed clusters.

2.2. MPGs Characterization

Scanning Electron Microscopy (JSM IT300, Peabody, MA, USA) was used to analyze the films of SiO₂ based artificial opals and MPGs deposited on glass substrates. We found that the opal matrix is made up of SiO₂ spheres with diameters within $275 \pm 10 \text{ nm}$ range. The spheres' sizes followed a Gaussian distribution. A cross-section analysis of an MPG beam provided a view of the random arrangement of the spheres due to the aggregation of Fe₃O₄ NPs. The NPs are predominantly spherical and have an average size of $20 \pm 4 \text{ nm}$. Magnetic properties were investigated using a Dyna Cool-9 with a vibrating sample magnetometer (VSM) module (Quantum Design, San Diego, CA, USA). This technique obtained a diameter of $19 \pm 1 \text{ nm}$ for the Fe₃O₄ NPs inside our sample, which is in excellent agreement with SEM results. An ultraviolet–visible–near-infrared spectrophotometer (Black Comet, Tampa, FL, USA) was utilized to obtain the specular reflection spectra from the MPGs. The reflection is measured at normal incidence with a 0.22 NA and cone angle of 25.4 degrees optical fiber. The optical resolution is less than 1 nm with a 25 μm slit.

We tested forced oscillations using the same experimental setup found elsewhere [37–39]. We used a laser Doppler vibrometer (VibroMet 500V MetroLaser, Irvine, CA, USA) to measure mechanical oscillations. In our experiments, the light-induced electromagnetic forces, consequently the MPG, oscillated at 69 Hz. The working wavelength $\lambda = 633 \text{ nm}$ of a He-Ne laser, with a power of 43 mW and a point size of approximately 1.65 mm^2 . A chopper acted as an on-and-off switch for the pumping He-Ne laser. The laser light impinged over the MPG with the help of a first surface reflection mirror. The vibrometer measured the mechanical oscillations, and the analog measurements were converted into digital and captured on a computer for further analysis.

2.3. FEM Numerical Simulations

We utilized full-wave finite element simulations with the help of FEMLAB 3.0 (Burlington, MA, USA), a commonly used simulation software in different engineering and scientific research fields. This software allows for single-physics and fully coupled multiphysics modeling potentialities, model management, and user-friendly tools that make it easy to create simulation applications. For the current study, we estimated the highest volumetric electromagnetic force density and input its value into the Plane Stress mode of the Structural Mechanical Module. The objective was to compute the maximum displacement induced by the magnetic force on a beam made of MPGs. The geometry we utilized is depicted in Figure 1. It consists of an MPG beam having 2 mm length, 825 μm width, and 10.47 μm thickness. All simulation parameters are displayed in Table 1.

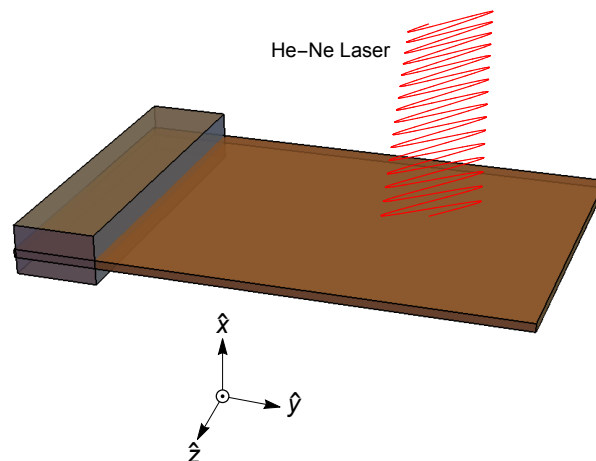


Figure 1. The geometry represents the magnetic glass studied here. It consists of an MPG beam of 2 mm length, 825 μm width, and 10.47 μm thickness. The incident light travels in the x-direction.

Table 1. The parameters for simulation that were employed in the Femlab 3.0 software are related to the Plane Stress application, which can be located within the Structural Mechanics Module.

Geometry	Material Properties	Constraints and Loads	Application Mode Parameters
Length of the beam: 2 mm. Width of the beam: 825 μm . Thickness of the beam: 10.47 μm . The volume of the beam: $17.3 \times 10^{-12} \text{ m}^3$.	The beam is considered linear and elastic with the following properties: Young's modulus: 55.34 GPa. Density: 2030.67 kg/m^3 .	The left end is fixed but the right end is free and subjected to a distributed load W per m^3 .	Default element type: Lagrange–Quadratic. Analysis type: Static
Mesh Parameters	Solver Parameters		
Mesh size: Normal. Number of degrees of freedom: 205,124. Number of Mesh points: 27,154. Number of triangular elements: 48,256. Triangle base length: 2.2 μm . Triangle height: 1 μm . Number of boundary elements: 6048. Number of vertex elements: 8. Minimum element quality: 0.7056. Element area ratio: 0.8030.	Analysis: Harmonic propagation Solver: Stationary. Linear system solver: Direct (UMFPACK). Relative tolerance: 10^{-6} Maximum number of iterations: 25.		

2.4. Mechanical Oscillations Theoretical Model

When illuminated, the MPG beam behaves as an oscillating system. It generates forced oscillations like a pendulum in a medium with viscous friction subject to a constant force [37,54,55]. The differential equation of this dynamical system is:

$$\begin{aligned}
 \ddot{x} + 2h\dot{x} + \omega_0^2 x &= \langle a_{x\max} \rangle_T, & jT < t < (n_{\text{force}} + j)T, \\
 \ddot{x} + 2h\dot{x} + \omega_0^2 x &= 0, & (n_{\text{force}} + j)T < t < (j + 1)T, \\
 j &= 0, \dots, n,
 \end{aligned} \tag{1}$$

where $\langle a_{x\max} \rangle_T = \langle F_{x\max} \rangle_T / m_{\text{beam}}$, m_{beam} is the beam mass, and $\langle F_{x\max} \rangle_T$ is the maximum electromagnetic force, h is a damping coefficient, ω_0 is the system's natural frequency, n_{force} defines the duty cycle (fraction of the period where the force is on), j is the number of cycles that the force is on and off, and T is the forced oscillation period. $\langle F_{x\max} \rangle_T$ can be obtained from theory or computer simulations, T , n_{force} , and m_{beam} are known parameters from the experiment, and h is a fitting parameter.

The natural frequency ω_0 is obtained using a clamped beam configuration shown in Figure 1. For that geometry, the MPG's system's inherent frequency is determined by $\omega_0 = \alpha_0^2 \sqrt{Et^2/12\rho_{\text{beam}}L^4}$, where $\alpha_0 = 1.875$ is related to the boundary conditions, E is Young's modulus, t is the beam thickness, L is the beam length and ρ_{beam} is the volumetric mass density [56]. The Young's modulus and volumetric mass density are obtained by a volumetric average of the MPG's components: silicon dioxide, magnetite, and air. Their values are displayed in Table 1.

3. Results

3.1. Scanning Electron Microscopy

Figure 2a shows a superficial (111) plane of the SiO₂ opal before the infill is grown. The (111) family planes are parallel to the glass substrate. The opal has good uniformity. However, the natural structure of opals is far short of an ideal FCC lattice due to some defects like sphere vacancies and dislocations. Figure 2b shows an MPG composed of SiO₂ spheres and infiltrated Fe₃O₄ NPs. As observed in Figure 2c,d, the lattice is distorted, resulting in a disordered arrangement of spheres. The local inhomogeneity increased during deposition, diminishing the composite's crystalline structure; what causes the disorder? Unlike in reference [48], the NPs are not coated with a tetramethylammonium hydroxide (TMAOH). TMAOH acts as a surfactant to Fe₃O₄ NPs by absorbing the cationic species in the surface OH groups, thus creating a net repulsion between them. This means that strong electrostatic attractions between Fe₃O₄ NPs cannot be prevented; hence, the appearance of agglomerations whereby the disorder is created.

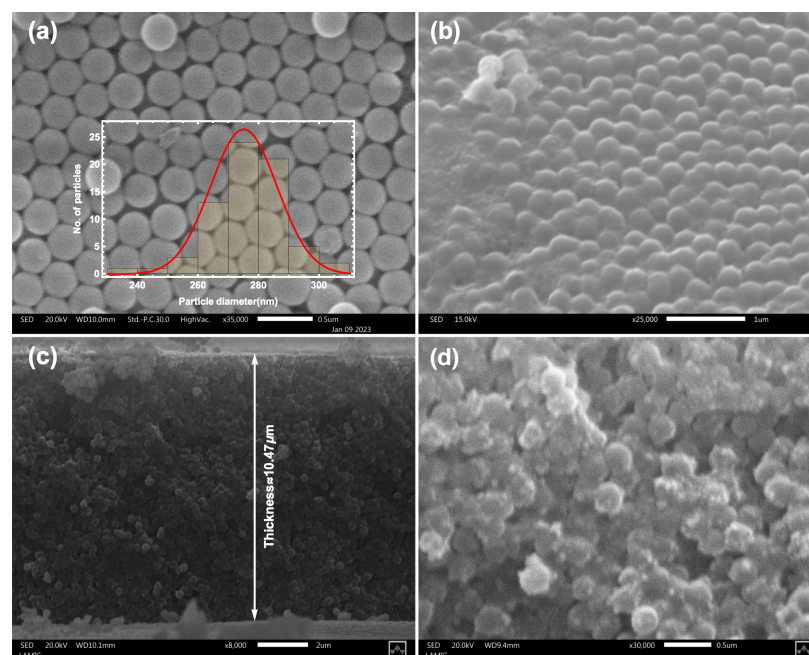


Figure 2. SEM image of an opal matrix composed of 275 ± 10 nm diameter SiO₂ spheres, before (a) and after (b) infiltration with Fe₃O₄ NPs. The size distribution histogram of spheres on the SiO₂ opal is shown in the inset. Panel (c) SEM image of a cross-section of an MPG beam where the random arrangement of the spheres is observed. Panel (d) shows an amplification of panel (c) and reveals that the aggregation of Fe₃O₄ NPs causes the disorder in the bulk.

Figure 3 shows an MPG beam with a length ranging from 1500 to 2000 μm and 10.47 μm thickness. The beam was built using adhesive tape applied over the MPG sample and lifted immediately. In this way, the beam is clamped at one end and free at the other. The clamped part is placed on the glass substrate. Superficial linear cracks formed by expansion during MPG's formation and drying of the wet structure can be observed. Over short distances, they often follow the crystallographic directions in opals [57].

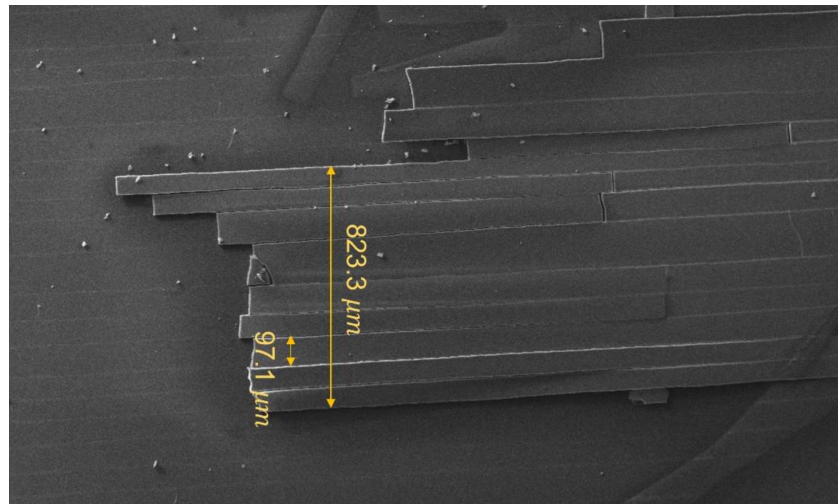


Figure 3. SEM image of an MPG beam, with a length of 1500–2000 μm and a thickness of 10.47 μm .

3.2. Magnetic Characterization

Magnetization measurements were conducted to study the magnetic behavior of the MPGs. The measurements were taken at room temperature and as a function of the applied magnetic field. Figure 4 shows the results; the absence of hysteresis and remanent magnetization indicates that the infiltrated magnetic NPs are in a superparamagnetic state [58]. The saturation magnetization value of the sample was 4.8 emu/g. This value was then normalized to the saturation magnetization for the bare Fe_3O_4 NPs (found to be 53 emu/g), and the Fe_3O_4 NPs concentration resulted in 9.05 wt %. Since the sample total mass is $m_T = 6.7 \times 10^{-3}$ g, then $m_{\text{Fe}_3\text{O}_4} = 6.06 \times 10^{-4}$ g, and $m_{\text{SiO}_2} = 6.09 \times 10^{-3}$ g. The Langevin function fitted the experimental data of magnetic particles' superparamagnetic behavior.

$$M(H/T) = M_0[\coth(M_0 m H / k_B T) - (k_B T / M_0 m H)], \quad (2)$$

where M_0 is the saturation magnetization in emu/g, m is individual particles' mass (in grams), and k_B is Boltzmann's constant. If we consider M_0 and m as fitting parameters, the values $M_0 = 4.8$ emu/g and $m = 180 \times 10^{-19}$ g are calculated at room temperature for the MPG. Taking into account the density of magnetite ($\rho_{\text{Fe}_3\text{O}_4}$) as 5.046 g/cm³, a diameter of 19 ± 1 nm was obtained for the Fe_3O_4 NPs, which is in excellent agreement with SME results.

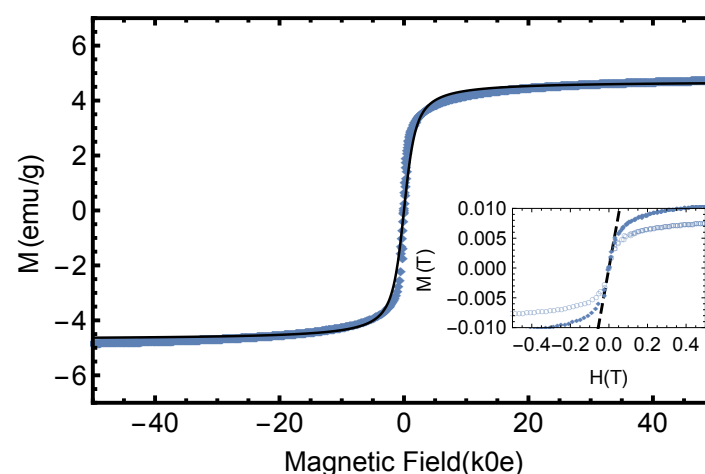


Figure 4. MPG magnetization hysteresis loops at 300 K with 9.05 wt % of Fe_3O_4 . The average SiO_2 sphere size is $D = 275$ nm. The inset shows the linear dependence of magnetization for low magnetic fields. The dark blue graph represents the forward direction, and the light blue represents the backward direction. The value of the slope is $\mu - 1 \simeq 0.2$.

To determine the real-valued permeability μ of the MPGs, we first calculate their densities using the expression:

$$\rho_{\text{beam}} = f_{\text{SiO}_2} \rho_{\text{SiO}_2} + f_{\text{Fe}_3\text{O}_4} \rho_{\text{Fe}_3\text{O}_4} + (1 - f_{\text{SiO}_2} - f_{\text{Fe}_3\text{O}_4}) \rho_{\text{air}}, \quad (3)$$

where $\rho_{\text{SiO}_2} = 2.65 \text{ g/cm}^3$.

The volume fractions for f_{SiO_2} , $f_{\text{Fe}_3\text{O}_4}$, and f_{air} can be approximated using Archimede's principle. Before the introduction of Fe_3O_4 NPs the total volume is $V_T = m_{\text{SiO}_2} / (0.74 \rho_{\text{SiO}_2})$, where we used the filling factor $f_{\text{SiO}_2} = 0.74$ corresponding to a compact structure of spheres. After Fe_3O_4 infiltration there is a volume expansion and the new volume V_{TA} is given by $V_T + V_d$, where V_d equals $m_{\text{Fe}_3\text{O}_4} / \rho_{\text{SiO}_2}$. Finally, the volume fractions are $f_{\text{SiO}_2} = m_{\text{SiO}_2} / (\rho_{\text{SiO}_2} V_{TA})$, $f_{\text{Fe}_3\text{O}_4} = m_{\text{Fe}_3\text{O}_4} / (\rho_{\text{Fe}_3\text{O}_4} V_{TA})$, and $f_{\text{air}} = 1 - f_{\text{SiO}_2} - f_{\text{Fe}_3\text{O}_4}$. Substituting all the needed experimental values the fractions are $f_{\text{SiO}_2} = 0.69$, $f_{\text{Fe}_3\text{O}_4} = 0.04$, and $f_{\text{air}} = 0.27$. We use ρ_{beam} to rescale the magnetization measurements in emu/cm^3 . So, by applying the conversion $795.7 \text{ emu/cm}^3 = 1 \text{ Tesla}$ and calculating H in Teslas, the measured slope value is $\mu - 1 = M/H \simeq 0.2$. The inset of Figure 4 illustrates the linear dependence of magnetization for a low applied magnetic field, indicating the value of that slope.

3.3. Optical Characterization

Figure 5 shows the reflection spectra of the as-prepared opals (dashed line) and MPGs that contain Fe_3O_4 NPs. Before the infiltration of Fe_3O_4 NPs, the presence of the observed band in the reflection spectra is attributable to Bragg diffraction from the (111) planes of the face-centered-cubic (fcc) opal lattice. We can estimate the average diameter of the SiO_2 spheres by calculating the position of the extremum of the diffraction line λ_{111} using Bragg's formula [59], given by:

$$\lambda_{111} = 2d_{111} \sqrt{\epsilon_{\text{opal}}}, \quad (4)$$

where $d_{111} = \sqrt{2/3} D$ is the interplanar distance within the opal, D is the average diameter of the SiO_2 spheres, and ϵ_{opal} is the opal's average dielectric constant

$$\epsilon_{\text{opal}} = f_{\text{SiO}_2} \epsilon_{\text{SiO}_2} + (1 - f_{\text{SiO}_2}) \epsilon_{\text{air}}, \quad (5)$$

For an opal structure, the filling factor $f_{\text{SiO}_2} = 0.74$ corresponding to a compact fcc lattice and the dielectric constants ϵ_{SiO_2} of the SiO_2 spheres have values of 2.13 [60]. Air dielectric constant ϵ_{air} equals one. For $\lambda_{111} \sim 600 \text{ nm}$, the average diameter of the SiO_2 spheres was found to be 275 nm, in agreement with measurements taken from SEM images.

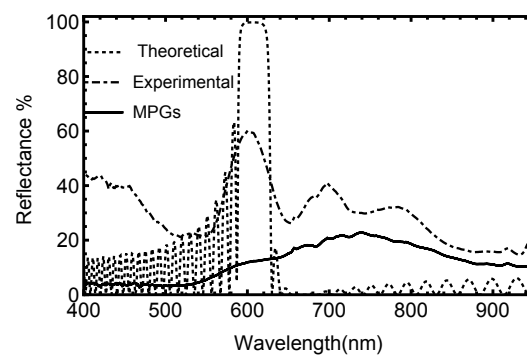


Figure 5. It presents the reflection spectra of an opal and MPG. The dashed line shows the reflection of a bare opal with a sphere size of $D = 275 \text{ nm}$; the highest peak is attributable to Bragg diffraction from the (111) planes of the face-centered-cubic (fcc) opal- SiO_2 based lattice. The solid line shows the reflection of the MPG having 4% of Fe_3O_4 . The dotted line represents the theoretical reflection spectrum from the (111) planes.

Equation (5) represents a higher bound for any effective dielectric constant for a medium with two components. The Weiner bounds provide one practical analytical constraint for the effective dielectric constant of a general photonic crystal, as in [61]. Specifically, for a two-material composite, each effective dielectric constant ϵ_α is bounded by

$$\left(f_1\epsilon_1^{-1} + f_2\epsilon_2^{-1}\right)^{-1} \leq \epsilon_\alpha \leq (f_1\epsilon_1 + f_2\epsilon_2), \quad (6)$$

where f_1 and f_2 are the volume fractions of the materials with dielectric constants ϵ_1 and ϵ_2 .

Equation (5) gives a value of 1.84; however, if we used a different effective medium approximation like Bruggeman [62], we obtained a value of 1.79 or Looyenga [63] gives 1.78, which is not that far from the Equation (5) value.

The optical losses deserve a comment. Since the cone angle is 25.4 degrees, any scattered light within that angle can be detected. Theoretically (Figure 5 dotted line), at 600 nm, the absorption losses for SiO₂ are negligible, but experimentally, there is a loss of about 40% of the optical power due to scattering. The 700 and 800 nm peaks might correspond to light coupling to diffraction bands presenting a low dispersion [64]. It has been forecasted [65] that within the frequency range where these bands exist, the photonic crystal operates (with regards to its optical response at normal incidence) as a medium with an effective refractive index, resulting in high reflectivity.

On the other hand, it can be observed that after infiltration of Fe₃O₄ NPs, the position of the maximum reflection experiences a redshift. The presence of disorder throughout the MPGs causes the attenuation of propagating light. Therefore, the reflection spectrum becomes less intense and asymmetric and may even broaden spectrally. To determine the average dielectric constant of the MPGs, we used the volume fractions calculated before and Looyenga's effective medium approximation as:

$$\epsilon_{\text{beam}} = (f_{\text{SiO}_2}\epsilon_{\text{SiO}_2}^{1/3} + f_{\text{Fe}_3\text{O}_4}\epsilon_{\text{Fe}_3\text{O}_4}^{1/3} + f_{\text{air}}\epsilon_{\text{air}}^{1/3})^3, \quad (7)$$

where the magnetite dielectric constant $\epsilon_{\text{Fe}_3\text{O}_4} = 5.56$ [66,67] is used. Then, a value of $\epsilon_{\text{beam}} = 1.86$ is obtained.

3.4. Mechanical Oscillations Measurements

The information on the experimental setup used to measure the oscillations of the beam based on an MPG is depicted in Figure 6. The laser light passes through the chopper and is reflected using a mirror to impinge perpendicularly on the sample. The laser Doppler vibrometer measures the oscillations, and the software interface provides data that includes the maximum displacement and velocity and the velocity time series, Fourier spectrum, and mean frequency.

Figure 7 shows the experimental results of oscillation measurements. The bare opal showed no significative and stable displacement (20 nm) at 140 Hz. However, there was no clear evidence of the oscillations for 69 Hz or any other explored frequency. On the contrary, the MPG oscillated significantly for a driven frequency of 69 Hz. Figure 7a shows the experimental results for the velocity time series, while Figure 7b displays its power spectral density (PSD). Figure 7c illustrates the maximum oscillation amplitude, velocity, and acceleration measured by the laser Doppler vibrometer. We found the maximum values for the displacement x_P and velocity v_P to be $x_P = 7.90 \mu\text{m}$ and $v_P = 3.42 \text{ mm/s}$ at 69 Hz. Additionally, the appearance of a second harmonic is observed. However, at 138 Hz, the sample did not show stable oscillations.

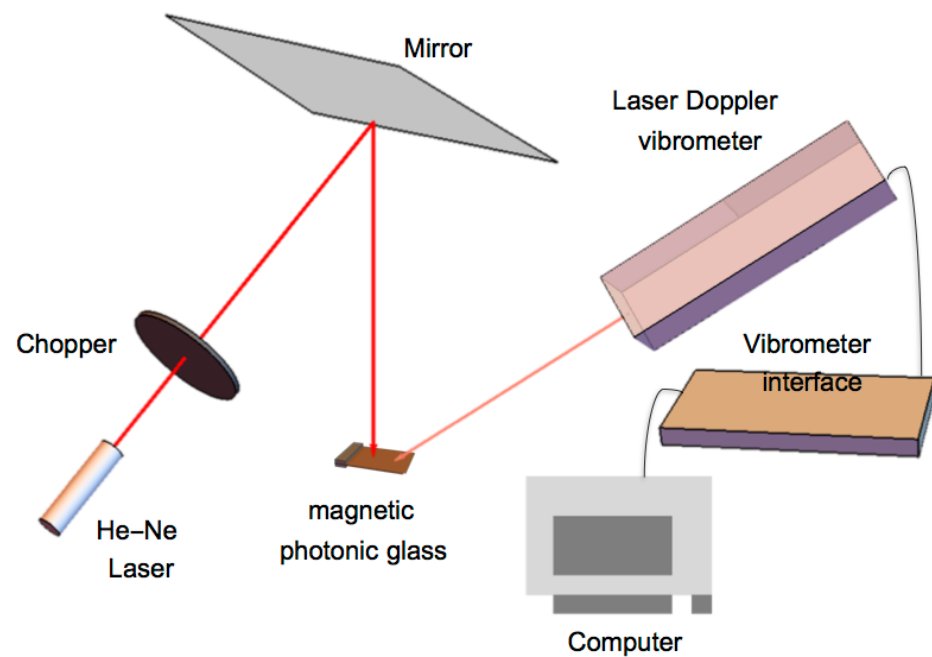


Figure 6. The equipment arrangement for measuring forced oscillations can be observed in the image. The setup includes components such as the He-Ne laser, mechanical chopper, MPG, laser Doppler vibrometer, vibrometer interface, and a computer. The chopper serves as a switch to control the pumping He-Ne laser. A first surface reflection mirror directs the laser light onto the MPG. Electromagnetic forces induced by the laser light cause the MPG material to oscillate at a frequency of 69 Hz, and the mechanical oscillations are measured using a laser Doppler vibrometer. The analog measurements are then converted into digital format and recorded on a computer for additional analysis.

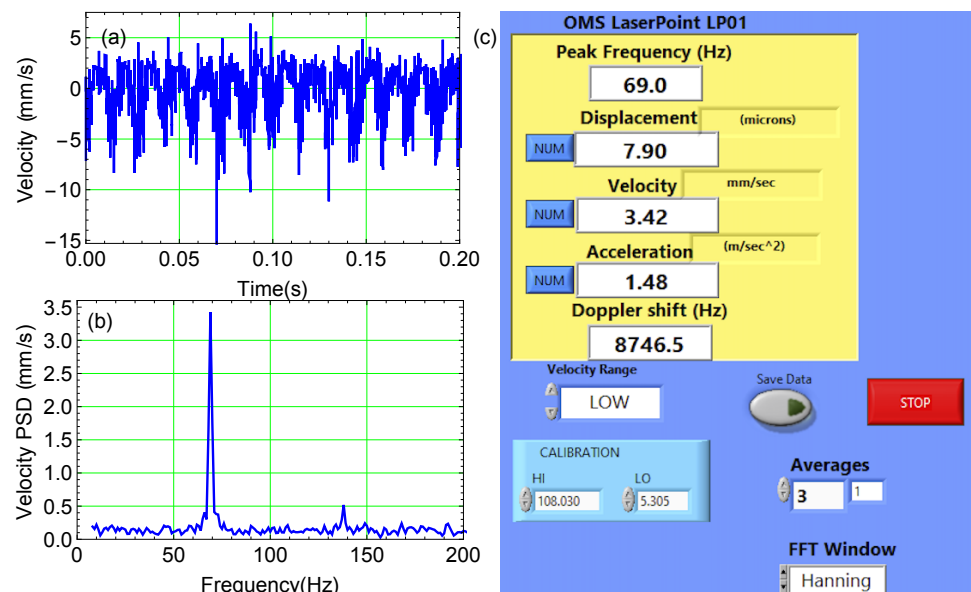


Figure 7. Forced oscillations experimental data at 69 Hz frequency. The data include a velocity time series (a) and its power spectral density plot (b), representing power distribution across different frequencies. Panel (c) shows the maximum displacement, velocity, and acceleration values.

3.5. FEM Numerical Simulations

The numerical simulations of the vibrating MPG are considered to interpret its induced magnetic force. Figure 8 displays the maximum oscillation amplitude. The simulation utilizes a distributed volumetric force density of $-2 \times 10^6 \text{ N/m}^3$. The minus sign for the force density is to consider that the electromagnetic wave impinges on top of the beam in the x-direction. The simulation resulted in a value of $8.02 \mu\text{m}$, close to the measured value of $7.9 \mu\text{m}$. From the maximum amplitude oscillation, we can infer the maximum oscillation velocity, which has a value of 3.43 mm/s . The value is close to the measured value of 3.42 mm/s .

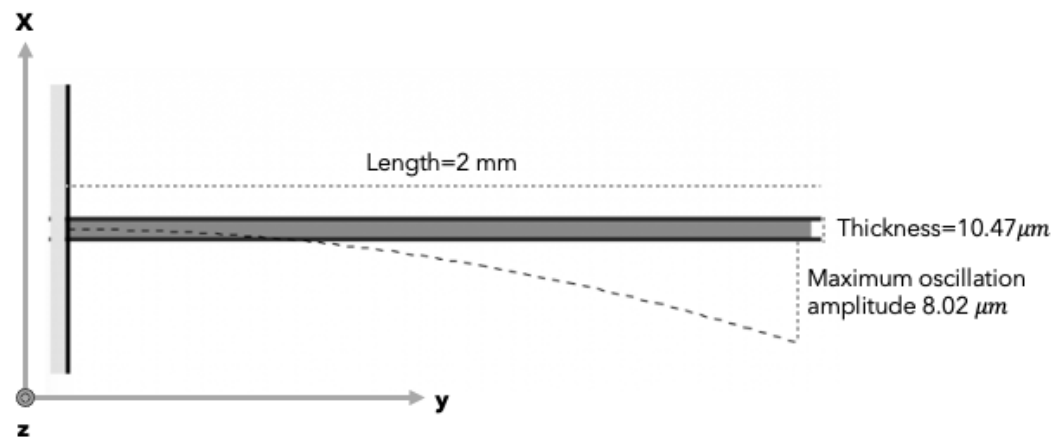


Figure 8. Maximum oscillation amplitude simulation. The force density is distributed volumetrically, and its magnitude is $-2 \times 10^6 \text{ N/m}^3$. The simulation is being done to determine the maximum amplitude of oscillation that can be achieved. The simulation result value of $8.02 \mu\text{m}$ is close to the measured value of $7.9 \mu\text{m}$.

3.6. Mechanical Oscillations Theoretical Model

To estimate the maximum induced acceleration $\langle a_{x\max} \rangle_T$ to the MPG, we used the maximum value of the induced electromagnetic force that equals the product of the volumetric force density times the MPG's volume or $(-2 \times 10^6) \times (1.73 \times 10^{-13}) \text{ N}$ or $-35 \mu\text{N}$. Using the MPG's volumetric mass density of 2030.67 kg/m^3 , and the MPG's volume of $1.73 \times 10^{-11} \text{ m}^3$ again, the mass m_{beam} is calculated to be $3.513 \times 10^{-8} \text{ kg}$. Therefore, the value for $\langle a_{x\max} \rangle_T$ is 935.33 m/s^2 . The value for ω_0 is $13,856.2 \text{ rad/s}$, we used the experimental value $n_{\text{force}} = 0.53$, and the damping coefficient h we found follows $h/w_0 = 8$. With these values, we simulated Equation (1) using Mathematica (Wolfram Research, Champaign, USA), and the best fit for the maximum displacement, velocity uses the value of $1.6\langle a_{x\max} \rangle_T$ for the acceleration. Consequently, the estimated maximum value of the induced electromagnetic force is $56 \mu\text{N}$. Since the FEM simulation does not consider any damping loss, it underestimates the value of such a force.

Figure 9 displays the simulated displacement and velocity time series, along with their PSD, which correlates well with the experimental measurements (refer to Figure 7). We added a zero-mean random noise to the simulated velocity time series to account for uncontrollable vibration effects.

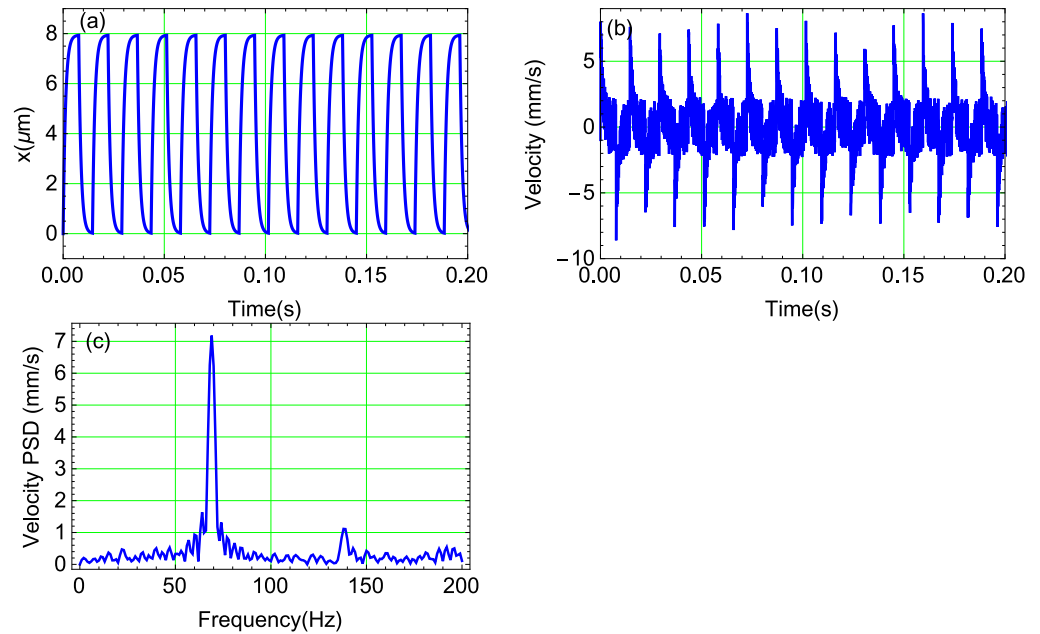


Figure 9. Forced-oscillation theoretical results for a frequency of 69 Hz. (a) Theoretical displacement time series. (b) Theoretical velocity time series and its (c) power spectral density.

4. Discussion

SiO₂-Fe₃O₄-based magnetic photonic glasses were synthesized, and films were prepared using a co-assembly method. Scanning Electron Microscopy (SEM) confirmed the glass's uniformity and structure. However, the lattice was distorted, resulting in a disordered arrangement of SiO₂ spheres when infiltrated with Fe₃O₄ NPs. Magnetic characterization demonstrated superparamagnetic behavior with increasing saturation magnetization, confirming the glass's magnetic properties. Optical characterization revealed a redshift in the reflection spectra after Fe₃O₄ infiltration. Moreover, the lattice distortion made the reflectance less intense and broadened.

Forced oscillation experiments at 69 Hz revealed significant displacement (7.9 μm) and velocity (3.42 mm/s) for the MPGs, demonstrating their responsiveness to external frequencies. The experimental setup and measurements were detailed, highlighting using a laser Doppler vibrometer for accurate displacement and velocity data.

The study utilized FEM simulations to estimate the volumetric electromagnetic force density, and the theoretical model refined its value. The model aligned well with experimental results, with the maximum oscillation amplitude and velocity closely matching the measured values. The theoretical model's parameters were estimated based on experimental data and simulations, supporting the validity of the theoretical framework. The simulated velocity time series and their power spectral density aligned well with experimental measurements, validating the theoretical predictions.

The combined experimental, numerical, and theoretical approach comprehensively shows the electromagnetic forces in MPG materials. This is our first attempt at achieving that force increment using magnetic dielectric materials. The nature of the mean force present in our system is magnetic, whose volumetric density is given by $\vec{f} = \nabla(\vec{M} \cdot \vec{B})$ where \vec{M} is the magnetization, and \vec{B} is the magnetic flux density.

5. Conclusions

This study focused on the induction of electromagnetic forces in MPG materials, particularly in a three-dimensional arrangement of SiO₂ spheres infiltrated with Fe₃O₄ NPs, considering light at 633 nm. In the past, the electromagnetic force could be increased by working with dielectric materials at a resonance state (localized photonic mode). Radiation pressures of the order 36.67 mN/m² and forces of 110 nN were achieved [38]; traditionally,

dielectric optomechanical photonic crystal cavities generate electromagnetic forces of the order of tenths of nN [40]. However, by adding a magnetic material, these forces can be increased 500-fold, as we have shown here. It is worth noting that the magnetic material helps improve the radiation pressure and stabilizes the structure mechanically. When Fe_3O_4 is inside the SiO_2 matrix, it remains stable for several hours, as demonstrated in our previous experiments with a dielectric material [37].

In the future, we need to maximize the gradient of $\vec{M} \cdot \vec{B}$, which implies using magnetic materials with higher magnetization and better geometrical designs that enhance the electromagnetic interactions. This study could expand the understanding of magnetic forces in MPGs, suggest potential applications in manipulating micro-objects through radiation pressure, and open avenues for further innovations. For example, by using sunlight instead of a laser in energy harvesters, the MPG oscillations induce voltages in a coil, and the energy can be stored.

Author Contributions: Conceptualization, M.A.P.-O., M.T.-S. and J.E.L.; methodology, M.A.P.-O., M.T.-S. and J.E.L.; software, M.T.-S. and J.E.L.; validation, B.F.D., R.P.-M., H.A.-S., A.J.C.-C., M.T.-S. and J.E.L.; formal analysis, M.T.-S. and J.E.L.; investigation, H.A.-S., A.J.C.-C., M.T.-S. and J.E.L.; resources, B.F.D., R.P.-M., M.A.P.-O., J.F. and J.E.L.; data curation, H.A.-S. and A.J.C.-C.; writing—original draft preparation, H.A.-S., M.T.-S. and J.E.L.; writing—review and editing, H.A.-S., A.J.C.-C., M.A.P.-O., B.F.D., R.P.-M., K.M., J.F., M.T.-S. and J.E.L.; visualization, H.A.-S., A.J.C.-C., B.F.D., R.P.-M., K.M. and J.E.L.; supervision, M.T.-S. and J.E.L.; project administration M.T.-S.; funding acquisition, J.F., M.T.-S. and J.E.L. All authors have read and agreed to the published version of the manuscript.

Funding: A Natural Sciences and Engineering Research Council of Canada Discovery #RGPIN-2022-05122 grant and the Mexican National Council funded this research for science and technology (no. CONACYT A1-S-38743).

Institutional Review Board Statement: Not applicable.

Informed Consent Statement: Not applicable.

Data Availability Statement: Data are contained within the article.

Conflicts of Interest: The authors declare no conflicts of interest. Jocelyn Faubert, Khashayar Misaghian, and J. Eduardo Lugo are the founders of Sage-Sentinel Smart Solutions. The paper reflects the views of the scientists and not the company.

References

1. Joannopoulos, J.D.; Johnson, S.G.; Winn, J.N.; Meade, R.D. *Photonic Crystals Molding the Flow of Light*; Princeton University Press: Princeton, NJ, USA; Oxford, UK, 2008.
2. Lugo, J.E.; Lopez, H.A.; Chan, S.; Fauchet, P.M.J. Porous silicon multilayer structures: A photonic band gap analysis. *Appl. Phys.* **2002**, *91*, 4966–4972. [[CrossRef](#)]
3. Fink, Y.; Winn, J.N.; Fan, S.; Chen, C.; Michel, J.; Joannopoulos, J.D.; Thomas, E.L. A dielectric omni-directional reflector. *Science* **1998**, *282*, 1679. [[CrossRef](#)] [[PubMed](#)]
4. Agarwal, V.; del Río, J.A.; Malpuech, G.; Zamfirescu, M.; Kavokin, A.; Coquillat, D.; Scalbert, D.; Vladimirova, M.; Gil, B. Photon Bloch oscillations in porous silicon optical superlattices. *Phys. Rev. Lett.* **2004**, *92*, 097401. [[CrossRef](#)]
5. Estevez, J.O.; Arriaga, J.A.; Mendez-Blas, A.; Reyes-Ayona, E.; Escorcía, J.; Agarwal, V. Demonstration of photon Bloch oscillations and Wannier-Stark ladders in dual-periodical multilayer structures based on porous silicon. *Nanoscale Res. Lett.* **2012**, *7*, 413.
6. Rodriguez, G.A.; Lawrie, J.L.; Weiss, S.M. *Porous Silicon Biosensors for DNA Sensing, Porous Silicon for Biomedical Applications*; Santos, H.A., Ed.; Woodhead Publishing Ltd.: Sawston, UK; University of Helsinki: Helsinki, Finland, 2014.
7. Lugo, J.E.; Doti, R.; Faubert, J. Negative refraction angular characterization in one-dimensional photonic crystals. *PLoS ONE* **2011**, *6*, e17188. [[CrossRef](#)]
8. John, S. Strong localization of photons in certain disordered dielectric superlattices. *Phys. Rev. Lett.* **1987**, *58*, 2486. [[CrossRef](#)] [[PubMed](#)]
9. Wu, F.; Lu, G.; Guo, Z.; Jiang, H.; Xue, C.; Zheng, M.; Chen, C.; Du, G.; Chen, H. Redshift gaps in one-dimensional photonic crystals containing hyperbolic metamaterials. *Phys. Rev. Appl.* **2018**, *10*, 064022. [[CrossRef](#)]
10. Wu, F.; Liu, T.; Xiao, S. Polarization-sensitive photonic bandgaps in hybrid one-dimensional photonic crystals composed of all-dielectric elliptical metamaterials and isotropic dielectrics. *Appl. Opt.* **2023**, *62*, 706–713. [[CrossRef](#)]

11. Park, J.M.; Gan, Z.; Leung, W.Y.; Liu, R.; Ye, Z.; Constant, K.; Shinar, J.; Shinar, R.; Ho, K.-M. Soft holographic interference lithography microlens for enhanced organic light emitting diode light extraction. *Opt. Express* **2011**, *19*, A786–A792. [[CrossRef](#)] [[PubMed](#)]
12. Matsubara, H.; Yoshimoto, S.; Saito, H.; Jianglin, Y.; Tanaka, Y.; Noda, S. GaN photonic-crystal surface-emitting laser at blue-violet wavelengths. *Science* **2008**, *319*, 445–447. [[CrossRef](#)]
13. Boroditsky, M.; Krauss, T.F.; Coccioli, R.; Vrijen, R.; Bhat, R.; Yablonovitch, E. Light extraction from optically pumped light-emitting diode by thin-slab photonic crystals. *Appl. Phys. Lett.* **1999**, *75*, 1036–1038. [[CrossRef](#)]
14. Nelson, E.C.; Dias, N.L.; Bassett, K.P.; Dunham, S.N.; Verma, V.; Miyake, M.; Wiltzius, P.; Rogers, J.A.; Coleman, J.J.; Li, X.; et al. Epitaxial growth of three-dimensionally architected optoelectronic devices. *Nat. Mater.* **2011**, *10*, 676–681. [[CrossRef](#)]
15. Lin, S.Y.; Moreno, J.; Fleming, J.G. Three-dimensional photonic-crystal emitter for thermal photovoltaic power generation. *Appl. Phys. Lett.* **2003**, *83*, 380–382. [[CrossRef](#)]
16. Yablonovitch, E. One-way road for light. *Nature* **2009**, *461*, 744–745. [[CrossRef](#)]
17. Wang, Z.; Chong, Y.; Joannopoulos, J.D.; Soljai, M. Observation of unidirectional backscattering-immune topological electromagnetic states. *Nature* **2009**, *461*, 772–775. [[CrossRef](#)] [[PubMed](#)]
18. Takahashi, K.; Kawanishi, F.; Mito, S.; Takagi, H.; Shin, K.H.; Kim, J.; Inoue, M. Study on magnetophotonic crystals for use in reflection-type magneto-optical spatial light modulators. *J. Appl. Phys.* **2008**, *103*, 07B331. [[CrossRef](#)]
19. Boriskina, J.V.; Erokhin, S.G.; Granovsky, A.B.; Vinogradov, A.P.; Inoue, M. Enhancement of the magnetorefractive effect in magnetophotonic crystals. *Phys. Solid State* **2006**, *48*, 717–721. [[CrossRef](#)]
20. Fedyanin, A.A.; Aktsipetrov, O.A.; Kobayashi, D.; Nishimura, K.; Uchida, H.; Inoue, M. Enhanced Faraday and nonlinear magneto-optical Kerr effects in magnetophotonic crystals. *J. Magn. Magn. Mater.* **2004**, *282*, 256–259. [[CrossRef](#)]
21. Lyubchanskii, L.; Dadoenkova, N.N.; Lyubchanskii, M.I.; Shapovalov, E.A.; Rasing, T. Magnetic photonic crystals. *J. Phys. D Appl. Phys.* **2003**, *36*, R277. [[CrossRef](#)]
22. Inoue, M.; Fujikawa, R.; Baryshev, A.; Khanikaev, A.; Lim, P.B.; Uchida, H.; Aktsipetrov, O.; Fedyanin, A.; Murzina, T.; Granovsky, A. Magnetophotonic crystals. *J. Phys. D Appl. Phys.* **2006**, *39*, R151. [[CrossRef](#)]
23. Zhang, H.F.; Liu, S.B.; Kong, X.K.; Li, B.X. Photonic band gap of three dimensional magnetized photonic crystal with Voigt configuration. *Eur. Phys. J.* **2013**, *67*, 169. [[CrossRef](#)]
24. Bahlmann, N.; Lohmeyer, M.; Zhuromskyy, O.; Dotsch, H.; Hertel, P. Nonreciprocal coupled waveguides for integrated optical isolators and circulators for TM-modes. *Opt. Commun.* **1999**, *161*, 330. [[CrossRef](#)]
25. Gevorgyan, A.H.; Golik, S.S.; Gevorgyan, T.A. Diode based on magneto-photonic crystals. *J. Magn. Magn. Mater.* **2019**, *474*, 173. [[CrossRef](#)]
26. Chen, J.; Liang, W.; Li, Z.Y. Strong coupling of topological edge states enabling group-dispersionless slow light in magneto-optical photonic crystals. *Phys. Rev. B* **2019**, *99*, 014103. [[CrossRef](#)]
27. Sheng, P. *Introduction to Wave Scattering, Localization, and Mesoscopic Phenomena*; Academic Press: San Diego, CA, USA, 1995.
28. van Albada M.P.; van Tiggelen, B.A.; Lagendijk, A.; Tip, A. Speed of propagation of classical waves in strongly scattering media. *Phys. Rev. Lett.* **1991**, *66*, 3132. [[CrossRef](#)]
29. Gottardo S.; Sapienza, R.; Garcia, P.D.; Blanco, A.; Wiersma, D.S.; Lopez, C. Resonance-driven random lasing. *Nat. Photonics* **2008**, *2*, 429. [[CrossRef](#)]
30. Schertel, L.; Siedentop, L.; Meijer, J.M.; Keim, P.; Aegerter, C.M.; Aubry, G.J.; Maret, G. The structural colors of photonic glasses. *Adv. Opt. Mater.* **2019**, *7*, 1900442. [[CrossRef](#)]
31. Schertel, L.; Wimmer, I.; Besirski, P.; Aegerter, C.M.; Maret, G.; Polarz, S.; Aubry, G.J. Tunable high-index photonic glasses. *Phys. Rev. Mater.* **2019**, *3*, 015203. [[CrossRef](#)]
32. Ashkin, A. Acceleration and trapping of particles by radiation pressure. *Phys. Rev. Lett.* **1970**, *24*, 156. [[CrossRef](#)]
33. Ashkin, A.; Dziedzic, J.M. Optical trapping and manipulation of viruses and bacteria. *Science* **1987**, *235*, 1517. [[CrossRef](#)] [[PubMed](#)]
34. Boales, J.A.; Mateen, F.; Mohanty, P. Micromechanical resonator driven by radiation pressure force. *Sci. Rep.* **2017**, *7*, 1. [[CrossRef](#)]
35. Metzger, C.H.; Karrai, K. Cavity cooling of a microlever. *Nature* **2004**, *432*, 1002–1005. [[CrossRef](#)]
36. Wilson-Rae, I.; Nooshi, N.; Zwerger, W.; Kippenberg, T.J. Theory of ground state cooling of a mechanical oscillator using dynamical backaction. *Phys. Rev. Lett.* **2007**, *99*, 093901. [[CrossRef](#)] [[PubMed](#)]
37. Lugo, J.E.; Doti, R.; Sánchez, N.; de la Mora, M.B.; del Río, J.A.; Faubert, J. The bifoil photodyne: A photonic crystal oscillator. *Sci. Rep.* **2014**, *4*, 3705. [[CrossRef](#)] [[PubMed](#)]
38. Lugo, J.E.; Doti, R.; Sánchez, N.; Faubert, J. Inducing forced and auto-oscillations in one-dimensional photonic crystals with light. *J. Nanophoton.* **2014**, *8*, 083071. [[CrossRef](#)]
39. Sánchez-Castro, N.; Palomino-Ovando, M.A.; Estrada-Wiese, D.; Valladares, N.X.; del Río, J.A.; De la Mora, M.B.; Lugo, J.E. The Influence of the External Signal Modulation Waveform and Frequency on the Performance of a Photonic Forced Oscillator. *Materials* **2018**, *11*, 854. [[CrossRef](#)] [[PubMed](#)]
40. Xia, J.; Qiao, Q.; Zhou, G.; Chau, F.S.; Zhou, G. Opto-mechanical photonic crystal cavities for sensing application. *Appl. Sci.* **2020**, *10*, 7080. [[CrossRef](#)]
41. Matamoros-Ambrocio, M.; Sánchez-Mora, E.; Gómez-Barojas, E.; Luna-López, J.A. Synthesis and study of the optical properties of PMMA microspheres and opals. *Polymers* **2021**, *13*, 2171. [[CrossRef](#)]

42. Norris, D.J.; Arlinghaus, E.G.; Meng, L.; Heiny, R.; Scriven, L.E. Opaline photonic crystals: How does self-assembly work? *Adv. Mater.* **2004**, *16*, 1393. [\[CrossRef\]](#)
43. Fudouzi, H.; Xia, Y. Photonic papers and inks: Color writing with colorless materials. *Adv. Mater.* **2003**, *15*, 892. [\[CrossRef\]](#)
44. Huang, C.K.; Chan, C.H.; Chen, C.Y.; Tsai, Y.L.; Chen, C.C.; Han, J.L.; Hsieh, K.H. Rapid fabrication of 2D and 3D photonic crystals and their inversed structures. *Nanotechnology* **2007**, *18*, 265305. [\[CrossRef\]](#) [\[PubMed\]](#)
45. Ye, J.; Zentel, R.; Arpiainen, S.; Ahopelto, J.; Jonsson, F.; Romanov, S.G.; Torres, C.M.S. Integration of self-assembled three-dimensional photonic crystals onto structured silicon wafers. *Langmuir* **2006**, *18*, 7378. [\[CrossRef\]](#) [\[PubMed\]](#)
46. Chan, C.H.; Chen, C.C.; Huang, C.K.; Weng, W.H.; Wei, H.S.; Chen, H.; Lin, H.T.; Chang, H.S.; Chen, W.Y.; Chang, W.H.; et al. Self-assembled free-standing colloidal crystals. *Nanotechnology* **2005**, *16*, 1440. [\[CrossRef\]](#)
47. Cong, H.; Yu, B.J. Fabrication of superparamagnetic macroporous Fe₃O₄ and its derivatives using colloidal crystals as templates. *Colloid Interface Sci.* **2011**, *353*, 131. [\[CrossRef\]](#)
48. Carmona-Carmona, A.J.; Palomino-Ovando, M.A.; Hernández-Cristobal, O.; Sánchez-Mora, E.; Toledo-Solano, M. Synthesis and characterization of magnetic opal/Fe₃O₄ colloidal crystal. *J. Cryst. Growth* **2017**, *462*, 6. [\[CrossRef\]](#)
49. Romero-Cruz, L.A.; Santos-Gómez, A.; Palomino Ovando, M.A.; Hernández Cristobal, O.; Sánchez Mora, E.; González, A.L.; Toledo Solano, M. Surface enhanced Raman scattering due to interstitial gold nanoparticles into SiO₂ spheres array. *Superlattices Microstruct.* **2018**, *123*, 71. [\[CrossRef\]](#)
50. Fang, M.; Volotinen, T.T.; Kulkarni, S.K.; Belova, L.; Rao, K.V. Effect of embedding Fe₃O₄ nanoparticles in silica spheres on the optical transmission properties of three-dimensional magnetic photonic crystals. *J. Appl. Phys.* **2010**, *108*, 103501. [\[CrossRef\]](#)
51. Shung, K.W.-K.; Tsai, Y.C. Surface effects and band measurements in photonic crystals. *Phys. Rev. B* **1993**, *48*, 11265. [\[CrossRef\]](#)
52. Mansuripur, M. Radiation pressure and the linear momentum of the electromagnetic field in magnetic media. *Opt. Express* **2007**, *15*, 13502. [\[CrossRef\]](#)
53. Sanchez-Seguame, G.; Avalos-Sanchez, H.; Eduardo Lugo, J.; Murillo-Bracamontes, E.A.; Palomino-Ovando, M.A.; Hernández-Cristobal, O.; Gervacio-Arciniega, J.J.; Toledo-Solano, M. Magnetic-Dielectric Cantilevers for Atomic Force Microscopy. *Nanomaterials* **2024**, *14*, 874. [\[CrossRef\]](#) [\[PubMed\]](#)
54. Andronov, A.A.; Vitt, A.A.; Khakin, S.E. *Theory of Oscillations*, 1st ed.; Princeton University Press: Princeton, NJ, USA, 1949; pp. 102–137.
55. Jenkins, A. Self-oscillation. *Phys. Rep.* **2013**, *525*, 2. [\[CrossRef\]](#)
56. Rabe, U.; Janser, K.; Arnold, W. Vibrations of free and surface-coupled atomic force microscope cantilevers: Theory and experiment. *Rev. Sci. Instruments* **1996**, *67*, 3281. [\[CrossRef\]](#)
57. Li, H.L.; Dong, W.; Bongard, H.J.; Marlow, F. Improved controllability of opal film growth using capillaries for the deposition process. *J. Phys. Chem. B* **2005**, *109*, 9939. [\[CrossRef\]](#) [\[PubMed\]](#)
58. Kulkarni, S.A.; Sawadh, P.S.; Palei, P.K.; Kokate, K.K. Effect of synthesis route on the structural, optical and magnetic properties of Fe₃O₄ nanoparticles. *Ceram. Int.* **2014**, *40*, 1945. [\[CrossRef\]](#)
59. Gajiev, G.M.; Golubev, V.G.; Kurdyukov, D.A.; Medvedev, A.V.; Pevtsov, A.B.; Sel'kin, A.V.; Tranikov, V.V. Bragg reflection spectroscopy of opal-like photonic crystals. *Phys. Rev. B* **2005**, *72*, 205115. [\[CrossRef\]](#)
60. Malitson, I.H. Interspecimen comparison of the refractive index of fused silica. *Josa* **1987**, *55*, 1205–1209. [\[CrossRef\]](#)
61. Aspnes, D.E. Local-field effects and effective-medium theory: A microscopic perspective. *Am. J. Phys* **1982**, *50*, 704–709. [\[CrossRef\]](#)
62. Bruggeman, D.A.G. Berechnung verschiedener physikalischer Konstanten von heterogenen Substanzen. *Ann. Phys.* **1935**, *416*, 636. [\[CrossRef\]](#)
63. Landau, L.D.; Lifshitz, E.M. *Electrodynamics of Continuous Media*; Pergamon Press: Oxford, UK, 1960.
64. Miguez, H.; Kitaev, V.; Ozin, G.A. Band spectroscopy of colloidal photonic crystal films. *Appl. Phys. Lett.* **2004**, *84*, 1239–1241. [\[CrossRef\]](#)
65. Sakoda, K. *Optical Characteristics of Photonic Crystals*; Springer-Verlag: Berlin, Germany, 2001.
66. Querry, M.R. *Optical Constants*, 1st ed.; University of Missouri-Kansas City: Kansas City, MO, USA, 1987; p. 17.
67. Han, R.; Li, W.; Pan, W.; Zhu, M.; Zhou, D.; Li, F.S. 1D magnetic materials of Fe₃O₄ and Fe with high performance of microwave absorption fabricated by electrospinning method. *Sci. Rep.* **2014**, *4*, 7493. [\[CrossRef\]](#)

Disclaimer/Publisher's Note: The statements, opinions and data contained in all publications are solely those of the individual author(s) and contributor(s) and not of MDPI and/or the editor(s). MDPI and/or the editor(s) disclaim responsibility for any injury to people or property resulting from any ideas, methods, instructions or products referred to in the content.